



Contents lists available at ScienceDirect

Nuclear Instruments and Methods in Physics Research A

journal homepage: www.elsevier.com/locate/nima

Characterization of thin-foil ultracold neutron detectors

A.L. Sallaska^{a,*}, S. Hoedl^a, A. Garcia^a, D. Melconian^b, A.R. Young^c, P. Geltenbort^d,
S.K.L. Sjue^a, A.T. Holley^c

^a University of Washington, Seattle, WA 98195, USA

^b Texas A&M University, College Station, TX 77843, USA

^c North Carolina State University, Raleigh, NC 27695, USA

^d Institut Laue-Langevin, 38042 Grenoble Cedex 9, France

ARTICLE INFO

Article history:

Received 5 November 2008

Received in revised form

30 January 2009

Accepted 8 February 2009

Available online 20 February 2009

Keywords:

Ultracold

Neutron

Detection

Detector

Cutoff velocity

Monte Carlo

Simulation

Lithium, Li

Boron, B

Lithium fluoride, LiF

Boron/Vanadium, B/V

Nickel, Ni

Rutherford

Scattering

Absorption

ABSTRACT

We have fabricated ultracold neutron detectors that consist of silicon charged particle detectors coupled with thin nickel foils coated with either natural LiF or ^{10}B implanted into vanadium. The foils convert neutrons into energetic, readily detectable, charged particles which are in turn detected by silicon detectors. The detectors were tested at the Institut Laue-Langevin with a gravitational spectrometer. From a rigorous Monte Carlo simulation of the experiment, the minimum detection cutoff velocities (effective potentials) were determined to be $309 \pm 17 \text{ cm/s}$ ($49.8 \pm 2.7 \text{ neV}$) for LiF and $367 \pm 39 \text{ cm/s}$ ($70.3 \pm 7.5 \text{ neV}$) for $^{10}\text{B/V}$. Although the result for LiF is consistent with expectations, the result for $^{10}\text{B/V}$ is significantly higher. We interpret this discrepancy as due to contamination. We also show that while a thicker foil is more efficient for ultracold neutron detection, a thinner foil is more ideal for determining the cutoff velocity.

Published by Elsevier B.V.

1. Introduction

Ultracold neutrons (UCNs) are used for a variety of experiments [1], including measurements of the neutron electric dipole moment [2], the neutron lifetime [3–5], and the neutron decay beta asymmetry [6–9]. A key problem for these experiments, however, is detecting the neutrons. In addition to being neutral, their energies are less than a few hundred neV, which cause them to reflect off a variety of materials at all angles of incidence. Therefore, neutrons will only be detected if they penetrate the surface (or surface window) of the detector. As detailed in Section 2, this will occur if the velocity of the UCN is greater than a “cutoff velocity,” defined by the effective potential barrier of the foil.

The conventional detection method employs ^3He proportional counters [10], which have some deficiencies. Besides being

cumbersome in size, leaks are a significant concern because of helium's large neutron capture cross section. In addition, these detectors are generally lowered to an inconvenient position below the beamline to ensure all the neutrons have velocities high enough to penetrate the window, which has a non-negligible cutoff velocity ($v_{\text{Al}} = 322 \text{ cm/s}$, $V_F = 54 \text{ neV}$).

As an alternative, solid state detectors coupled with charged particle converter foils are quite small, relatively simple to produce, and have a negligible background. Since evaporations and implantations necessarily imply some level of contamination, an important concern is producing foils that yield effective cutoff velocities low enough to detect a significant fraction of UCNs. Converter foils of ^6LiF and ^{10}B have been previously tested by other groups at the Institut Laue-Langevin (ILL) [11]. In addition, ^6Li and Ti multilayer foils have also been produced in an attempt to further decrease the cutoff velocity [12,13].

The cutoff velocities for compounds can be calculated using the elements' scattering lengths. However, in practice, contamination can result in significantly different values, and an experimental

* Corresponding author. Tel.: +1 206 543 4032; fax: +1 206 685 4634.

E-mail address: sallaska@u.washington.edu (A.L. Sallaska).

determination is necessary. This paper presents a quantitative determination of the cutoff velocity for evaporated naturally abundant LiF and ^{10}B implanted into vanadium. The LiF and $^{10}\text{B}/\text{V}$ detectors' properties are described, and the gravitational spectrometer at the ILL is detailed along with Monte Carlo simulations used to determine the foils' cutoff velocities.

2. Detectors

2.1. Converter foil plus charged particle detector setup

Fig. 1 shows a sketch of the conversion foil-detector setup, and Fig. 2 shows a photograph of a typical foil-detector assembly. For each type of converter foil, Ortec B Series silicon surface barrier detectors with an active area of 300 mm^2 were utilized. Upon capturing a neutron, the converter foil produces charged particle pair which are emitted back to back, allowing only one to be detected. Each foil was contained in a detachable holder mounted to the housing for the silicon detector and had a diameter of 1.6 cm. Because each component was mounted separately for convenience and versatility, the distance between the face of the silicon and the foil was 1.0 cm, yielding a solid angle of 11.9%, determined by simulation.

Nickel was chosen as the substrate because its high nuclear potential ($v_{\text{Ni}} = 695\text{ cm/s}$, $V_F = 252\text{ neV}$) allows a large fraction of UCNs to reflect and have a second chance to interact. The foils of approximately $1\text{ }\mu\text{m}$ of nickel were mounted on the frame by being placed between the main foil holder and a square top cover which was bolted on.

2.2. Converter materials

Materials that provide the conversion to detectable charged particles must have a low nuclear potential in conjunction with a large neutron capture cross section. An important feature of the foils is the cutoff velocity, below which the neutrons are reflected and cannot be absorbed. This is related to the scattering length

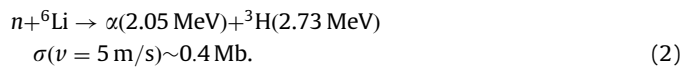
and Fermi potential, V_F [1], by

$$V_F = \frac{2\pi\hbar^2}{m_n} Na = \frac{1}{2} m_n (v_r^2 + i v_i^2) \quad (1)$$

where N is the volume density of the atoms of the material, m_n is the neutron mass, a is the complex scattering length, and v_r and v_i are the real and imaginary cutoff velocities, respectively. In our analysis, v_i was set by the absorption cross section, and v_r was the parameter to be determined. We chose to investigate two conversion materials: natural LiF and ^{10}B implanted into vanadium. For LiF, the calculated value of v_r is 320 cm/s ($V_F = 53.4\text{ neV}$) [14], which is nearly identical to that of the conventional window material for ^3He detectors, aluminum. These foils should perform no better than helium detectors in terms of their ability to detect low energy UCNs but have the advantages described in the introduction. The $^{10}\text{B}/\text{V}$ foils we fabricated have a lower calculated cutoff of 120 cm/s ($V_F = 7.5\text{ neV}$) [15], making them more attractive for use as UCN detectors.

2.2.1. Lithium fluoride foils

The natural LiF foils capture neutrons via the reaction



Natural LiF instead of ^6Li was employed for multiple reasons: the fluorine ensured the stability of the foil, and the negative scattering length of ^7Li , -2.2 fm , canceled the positive scattering length of ^6Li , 2.0 fm , thus minimizing the cutoff velocity. These foils were fabricated by resistively evaporating $640\text{ }\mu\text{g}/\text{cm}^2$ of LiF onto $900\text{ }\mu\text{g}/\text{cm}^2$ nickel foils.

In order to have the cleanest depositions, the bell jar pressure was kept in the range of high 10^{-7} Torr to low 10^{-6} Torr. Also, to avoid breaking the foils, the temperature of the boat containing the LiF was kept as low as possible, which allowed the deposition to be completed in $\sim 8\text{ h}$. A typical ionization spectrum from a silicon detector with a LiF foil illuminated with UCNs is shown in Fig. 3, illustrating the cleanly resolved triton peak. To minimize backgrounds, our energy cut contained only this peak.

2.2.2. Boron and vanadium foils

The $^{10}\text{B}/\text{V}$ foils capture neutrons via the reactions

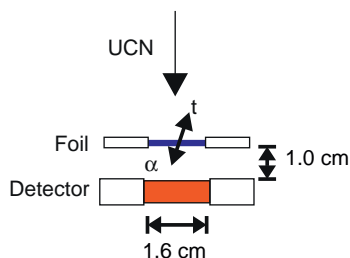
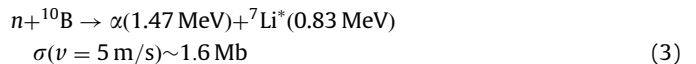


Fig. 1. Scheme of detector setup.

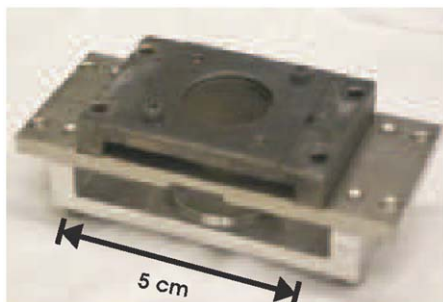


Fig. 2. Photograph of detector.

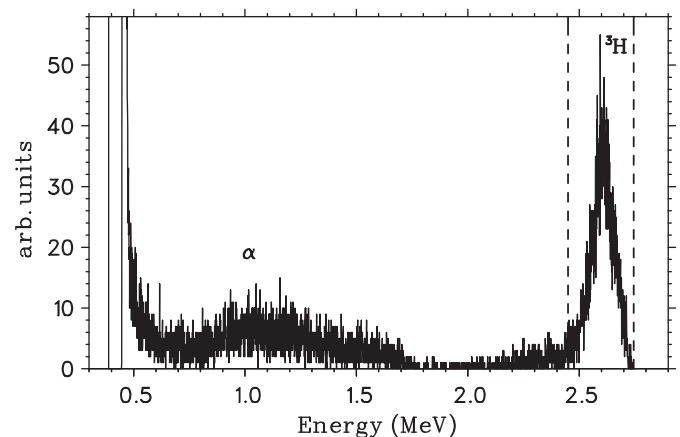


Fig. 3. Energy spectrum observed with a LiF foil, including cuts.

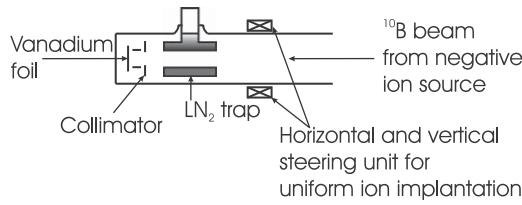
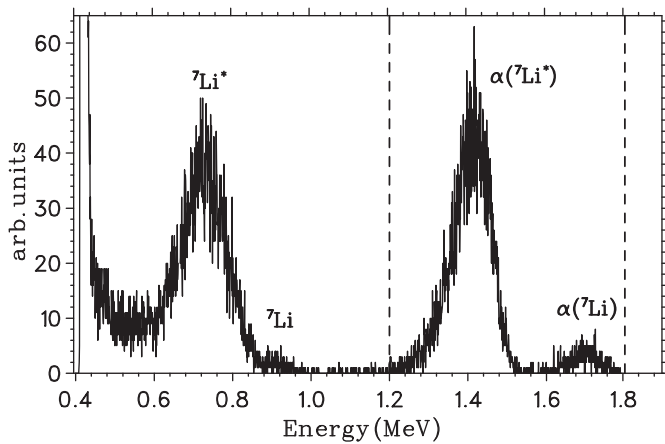


Fig. 4. Implantation setup.

Fig. 5. Energy spectrum observed with a $^{10}\text{B}/\text{V}$ foil, including cuts. The highest energy peaks correspond to detection of alphas and the lowest ones to detection of ^7Li .

$$n + {}^{10}\text{B} \rightarrow \alpha(1.78 \text{ MeV}) + {}^7\text{Li}(1.01 \text{ MeV})$$

$$\sigma(v = 5 \text{ m/s}) \sim 0.1 \text{ Mb.} \quad (4)$$

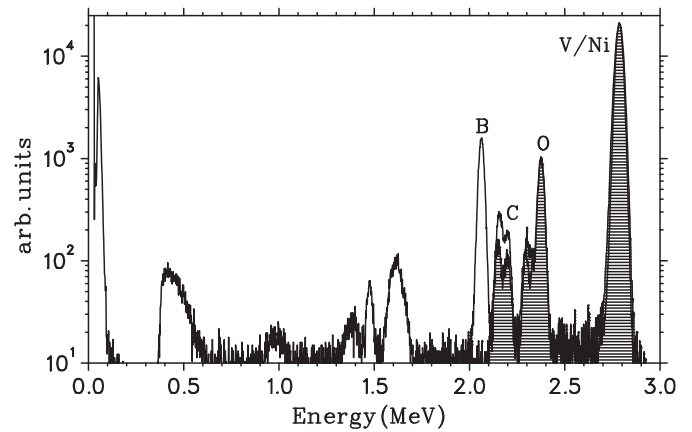
The foils were produced by evaporating vanadium with an electron beam onto the $\sim 1 \mu\text{m}$ thick nickel foils, after evaporating a 10 nm chromium adhesion layer. Then, using a negative ion source at the University of Washington, approximately 10^{18} ^{10}B atoms were ion-implanted into the vanadium at an energy of 80 keV, which yields a depth of $\sim 200 \text{ nm}$. A sketch of the ion implantation setup is shown in Fig. 4.

In order to produce uniform implantations, the beam was scanned through the foil by a computer-controlled magnetic steering unit. The beam diameter was $\sim 2 \text{ mm}$, and the scan diameter was $\sim 1.5 \text{ cm}$. The beam was scanned through the target in 2 h utilizing an elliptical pattern, and the implantations typically ran for 2 days.

Fig. 5 illustrates the ionization spectrum from a solid state detector with UCNs impinging on a $^{10}\text{B}/\text{V}$ foil. We observe the expected ionization spectrum showing peaks corresponding to α and ^7Li particles, leaving the latter in its ground or first excited state. As with the LiF foil, the higher energy peaks were chosen for the energy cuts to minimize backgrounds.

3. Backscattering to determine surface density

An important parameter in the Monte Carlo simulations was the surface density or thickness of the neutron absorber on the foils. It determines the detection efficiency, which also depends on the absorption cross section and cutoff velocity. Throughout fabrication, the densities were monitored by integrating the beam current during implantation or by measuring a frequency change on a crystal thickness monitor during evaporation. At the time of fabrication, we were not concerned with the exact number of

Fig. 6. Spectrum of scattered 3 MeV protons observed with a $^{10}\text{B}/\text{V}$ foil at $\theta = 150^\circ$. The shaded region is a spectrum taken with a blank nickel foil. This clearly indicates carbon as the dominant contaminant arising from implantation.

atoms deposited; however, during the analysis it became clear that the neutron absorber density played a critical role.

In order to more accurately determine the densities of the foils, elastic backscattering measurements were performed at the University of Washington with 1 and 3 MeV protons. These energies were chosen so that the energy loss in the target did not exceed the energy difference between the elastic-scattering peaks. In a 24 in. cylindrical chamber, two 500 μm Canberra Passivated Implanted Planar Silicon (PIPS) detectors [16] were placed each at 150° with respect to the proton beam and were shielded from multiple scatters by aluminum caps wrapped around the detector and its two collimators. Using information from the peaks in the spectrum, the densities could be determined given the known cross sections via

$$\frac{N}{\Delta t} = \left(\frac{I}{e} \right) \left(\frac{d\sigma}{d\Omega} \right) d\Omega f \rho_A \quad (5)$$

where $N/\Delta t$ is the observed rate, I is the beam current, $d\Omega$ is the solid angle, f is the correction due to dead time, and ρ_A is the surface density. Dead time was measured by the ratio of counts from a pulser signal in one of the detector's preamps to the pulser fed directly into a scaler. For some foils and energies, this correction was substantial, ranging from 11% to 57%. The $\sim 100 \text{ nA}$ current yielded data sets for each foil in under an hour.

A $87 \pm 4 \mu\text{g}/\text{cm}^2$ thick carbon foil served as a calibration to accurately determine the solid angle. At our proton energies, the carbon elastic scattering cross section has a non-Rutherford component; therefore, there was an associated uncertainty in determining the solid angle due to uncertainties in the carbon elastic cross sections [17]. Finally, a beam current integrator was used to extract the total number of incident protons during a given run. A sample spectrum at 3 MeV for each of the foils can be seen in Figs. 6 and 7, although data at 1 MeV were also used to determine the final density for ^{10}B . The resulting densities were $13.3 \pm 3.3 \mu\text{g}/\text{cm}^2$ for ^{10}B and $(6.4^{+1.3}_{-1.1}) \times 10^2 \mu\text{g}/\text{cm}^2$ for LiF . The uncertainties arise from both uncertainties in the solid angle and in the cross section for each reaction [18,19].

4. Characterization at the ILL

A gravitational spectrometer was used at the ultracold neutron installation PF2 of the ILL to characterize the performance of our UCN detectors. The concept behind the gravitational spectrometer was to change the velocity distribution at the detector by altering the net gravitational barrier that the neutrons must overcome.

Decreasing this barrier in turn decreased the minimum velocity needed to reach the detector.

UCNs traveled from the Steyerl turbine into the PF2/EDM beamline where this experiment was placed [20]. The neutrons then entered the gravitational spectrometer through a spectrum “shaper,” a sketch of which can be seen in cross section in Fig. 8. Built by Morozov and colleagues [21] from the Kurchatov Institute, the shaper addresses the well-known problem that the spectrum of neutrons exiting the guides at the ILL contains a large number of neutrons with velocities too high to be treated as UCNs [20]. It was made entirely from stainless steel, as were the rest of the experimental components. Its geometry of grids and tunnels forced the neutrons to collide numerous times with the outer walls, thereby filtering out UCNs with velocities higher than that of the guide material’s cutoff ($v_{ss} = 600$ cm/s,

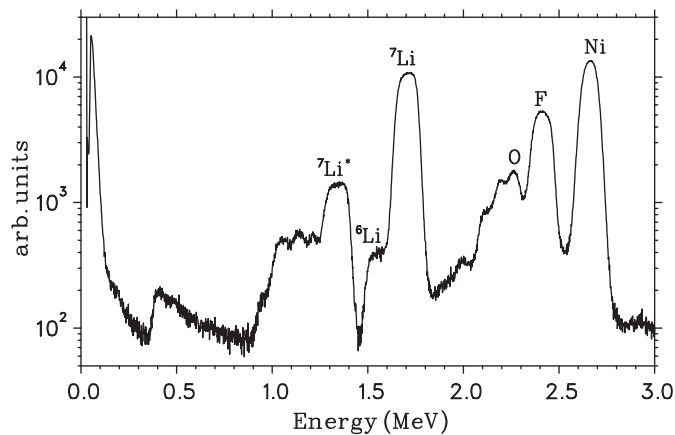


Fig. 7. Spectrum of scattered 3 MeV protons observed with a LiF foil at $\theta = 150^\circ$.

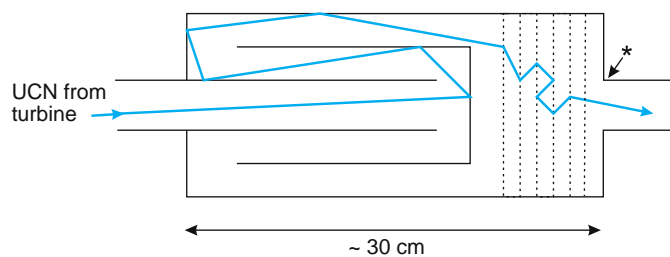


Fig. 8. A schematic of the shaper. The star corresponds to the position at which we calculated the final velocity spectra shown in Fig. 12.

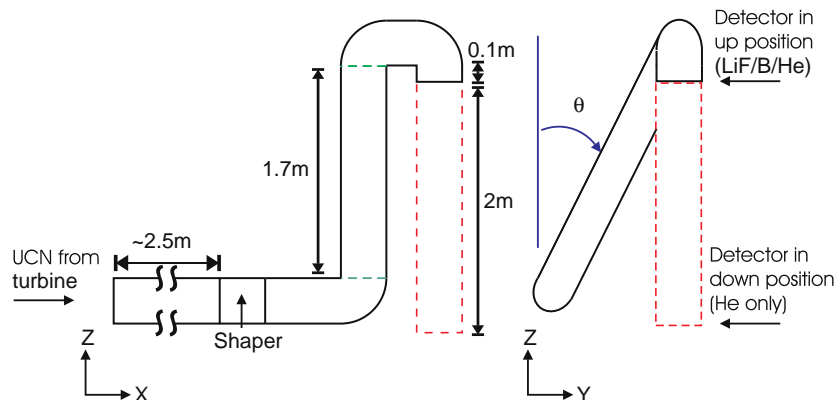


Fig. 9. A schematic of the gravitational spectrometer experimental setup.

$V_F = 187.9$ neV). This produced a well-defined maximum velocity in the distribution.

The entire setup is illustrated in Fig. 9. After exiting the shaper, the neutrons traveled up a pipe 170 cm in length, which in the $\theta = 0^\circ$ position required a minimum velocity of 570 cm/s to overcome the gravitational barrier. If they reached the top, the UCNs were then free to fall 13 cm to the detectors. The beam pipes were fabricated from stainless steel tubes used by the milk industry and included three 90° curved bends. To aid in the analysis, a helium detector was used at the same position as the solid state detectors and also at 200 cm below that position, connected by an additional section of stainless steel guide. The second position allowed the UCNs to be accelerated to velocities well above the aluminum window cutoff ($v_{Al} = 322$ cm/s, $V_F = 54$ neV). In this setup, a collimator was fabricated out of one of the empty foil holders to ensure that the helium detectors had the same acceptance area as the LiF and $^{10}\text{B}/\text{V}$ detectors. A neutron absorber made of TPX[®] (a plastic that turns out to have a very low effective potential) filled the beam pipe around the collimating holder to block any UCNs that did not hit the holder itself.

In order to change the minimum velocity required to reach the top, the vertical beam pipe was rotated around the horizontal guide from which the UCNs entered (x -axis shown in Fig. 9) by an angle θ . This was performed without changing any neutron guide components and while maintaining the detector’s vertical orientation. Results for the helium detector in both positions

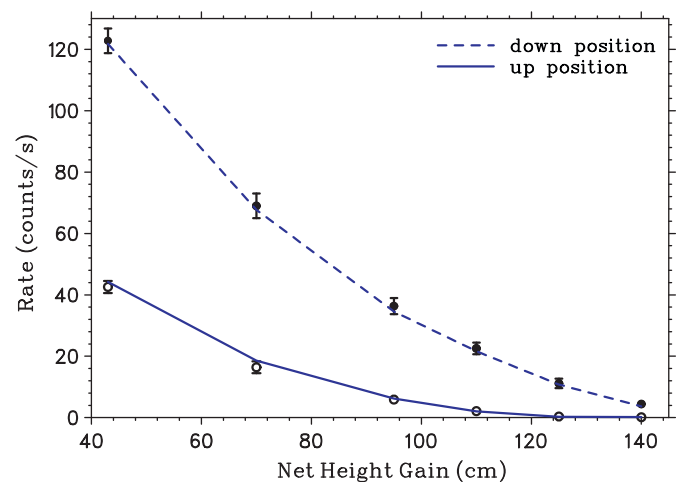


Fig. 10. Helium detector data points with Monte Carlo calibration curves. A net height gain of 140 cm corresponds to $\theta = 0^\circ$ shown in Fig. 9.

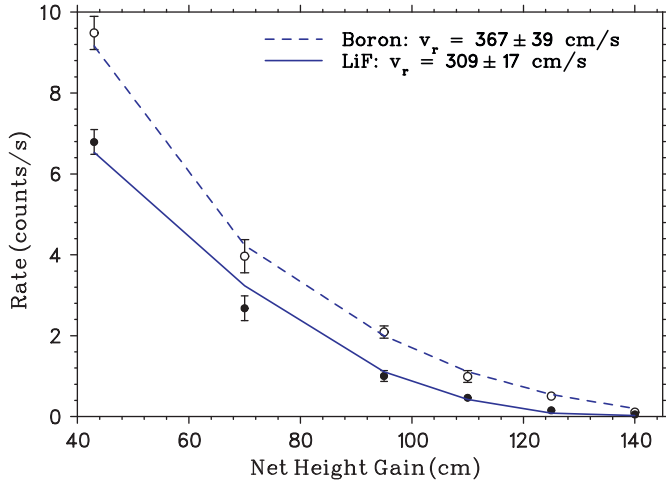


Fig. 11. LiF and $^{10}\text{B}/\text{V}$ data points with Monte Carlo results. A net height gain of 140 cm corresponds to $\theta = 0^\circ$ shown in Fig. 9.

and for the LiF and $^{10}\text{B}/\text{V}$ detectors are in Figs. 10 and 11, respectively.

These graphs plot the count rate as a function of net height gain along with our Monte Carlo results, which will be explained in the next section. The net height gain is the vertical distance from the horizontal beam pipe to the position of the detector. Each rate was calculated by dividing the total number of events between the energy cuts, as shown by the dotted lines in Figs. 3 and 5 for the LiF and $^{10}\text{B}/\text{V}$ detectors, respectively, by the total exposure time. A background correction was applied to each position of the helium detector by measuring the detection rate with the UCN source valved off. The correction ranged from 0.3% at the 43 cm position to 75% at the 140 cm position. As expected, the background rate was negligible in the solid state detectors. The uncertainties include counting statistics and a ± 2 cm uncertainty in the measured height, which can be seen as its estimated contribution to the rate shown in Figs. 10 and 11.

5. Analysis

The goal of the analysis was to reproduce the data with a Monte Carlo simulation and thus estimate the real part of the cutoff velocity for each foil, v_r . Since all detector setups were illuminated with the same neutrons, we imposed the stringent condition of reproducing *all* data with a unified set of parameters, hence providing a self-consistent test of our method. The simulation transported the neutrons by combining the algebraic expressions for the geometry (cylinders, grids, baffles) with the kinematic equations of motion to determine where and when the neutron's trajectory intersected the guide or detector. Then the neutron was either absorbed or reflected. The probability of reflection on surfaces was given by the exact quantum mechanical solution for a complex step potential [21]:

$$R(v, v_r, v_i) = 1 - \frac{2\sqrt{2}v(v^2 - v_r^2 + (v_i^4 + (v^2 - v_r^2)^{1/2})^{1/2})}{v^2 + (v_i^4 + (v^2 - v_r^2)^{1/2})^{1/2} + \sqrt{2}v(v^2 - v_r^2 + (v_i^4 + (v^2 - v_r^2)^{1/2})^{1/2})} \quad (6)$$

where v is the normal component of the neutron velocity, v_r is the cutoff velocity, and v_i is the imaginary cutoff velocity that parameterizes the absorptive property of the surface. The UCN could be reflected either diffusively or specularly. In a specular reflection, the normal component of the UCN velocity reversed sign; in a diffuse reflection, the UCN velocity vector was described

by a $\cos^2 \theta_f$ probability distribution, where θ_f was the angle to the surface normal after reflection. The probability of diffusive scatters was assumed to be $(1 - p_g) \cos \theta_i$, where θ_i was the initial angle of the UCN to the surface normal, and p_g was a constant of each section of the spectrometer which characterizes the specularity, or smoothness, of the surface [22].

If the neutron intersected an external guide wall and did not reflect, it was assumed to have been absorbed. However, if the barrier was not external, as in the shaper, absorption was determined from the absorption cross section, the volume density of the material, and the time spent in the material calculated from the neutron's velocity, which was shifted due to the non-zero potential of the material. If the neutron was not absorbed, it was allowed to continue into the system. Transport through the simulation ended when the neutron was either absorbed into guide components or was detected.

At the entrance to the shaper, the initial distribution was $v^2 dv$ up to a maximum velocity of 850 cm/s and was highly forward peaked with an isotropic azimuthal spread up to 3° , which was determined by our simulation as described. 850 cm/s was chosen as the maximum velocity to minimize simulation time; subsequent tests confirmed this choice by indicating that for initial velocities between 850 and 1000 cm/s, the fraction of neutrons reaching the top of the apparatus was less than 3×10^{-7} . In fact, only 1.6% of neutrons exiting the shaper had velocities above the shaper's cutoff. The grids themselves were modeled as planes where the probability of a collision was proportional to the area covered by stainless steel, 32%. If scattered, the neutron's angle was then oriented randomly from the surface normal.

Fig. 12 illustrates the effect of the shaper on the neutrons' velocity distributions. The bold faced curves are the initial, highly forward peaked velocity distributions, rescaled for clarity. The final spectrum represents the neutrons exiting the shaper and entering the subsequent system for the first time (see the star shown in Fig. 8). As evidenced by the final distribution, the shaper is an excellent velocity filter and also does a fair job of spreading out the angular distribution. Two features worth noting are the low yield of neutrons with velocities between 400 and 600 cm/s and the slight augmentation of neutrons at lower velocities. The former feature arises after the first bend of the guide where only neutrons with large enough angles were accepted into the system. The latter originates from distortions of the spectrum due to gravity.

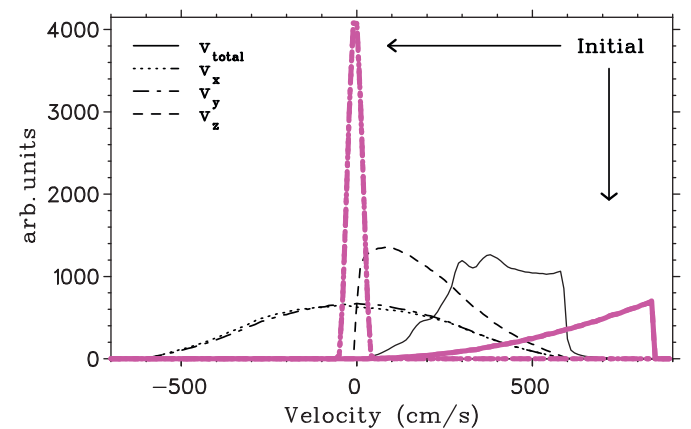


Fig. 12. Initial and final velocity spectra in the shaper for each component and also for the total velocity. x and y are transverse directions, and z is aligned axially along the guide. The initial spectrum is in bold and has been scaled by a factor of 50, with transverse velocity curves overlapping and with the total and axial velocities nearly overlapping.

Table 1
Simulation parameters.

Specularity constant		Reflection parameters		
Guide	p_g	Material	v_r (cm/s)	v_i (cm/s)
Shaper	0.95	SS	600	5.5
Straight guides	0.90	Al	322	1.4
Curved guides	0.775	TPX [®]	0.0	1.8
		LiF	309 ± 17 (calculated: 320 [14])	24.6
		¹⁰ B/V	367 ± 39 (calculated: 120 [15])	145.8

Included are the specularities for various guide components and the inputs to Eq. (6): real velocity cutoffs along with their imaginary cutoffs, which correspond to absorption. Results for the LiF and ¹⁰B/V foil real cutoffs are given, in addition to their values calculated from Eq. (1).

The experimental geometry was simplified somewhat for the Monte Carlo, in which each 90° bend was approximated by three short straight sections. Values of real and imaginary cutoffs for all materials, except the neutron detector foils, were assumed to be constant, given by their calculated values. Values of each relevant parameter, determined by simulation and explained in the next section, and the calculated values of the complex material potentials are given in Table 1. A specularity of 25% was used for the helium detector's aluminum window, and the collimator specularity was 75%; however, the best fits were fairly insensitive to these values, as were the LiF and ¹⁰B/V cutoff velocities to the foil specularity which was set to 90%. The extra pipe used with the helium detector in the “down” position was set to 100% specularity. The effect of lowering this value simply increased the value of the χ^2 but left the best fit parameters unchanged.

In order to illustrate the physical effect of the extracted specularity values, a simulation of a 100 cm horizontal section of stainless steel guide was performed. With an initial $v^2 dv$ velocity distribution up to the stainless steel cutoff and an isotropic angular distribution, the average number of diffusive scatters per bounce was 0.035 for $p_g = 0.95$, 0.069 for $p_g = 0.90$, and 0.154 for $p_g = 0.775$. Due to numerical losses, a fraction of 5×10^{-6} neutrons are removed from the simulation, of which 71% are lost in the shaper alone.

The Monte Carlo simulation modeled the full geometry of the neutron detectors. For the helium detector, the geometry included the TPX[®] and empty foil holder collimators, and the structure of the aluminum entrance window, which was supported by six 4 mm baffles. For the LiF and ¹⁰B/V detectors, the geometry included the full foil holder apparatus. For all detectors, the neutrons must first penetrate the foil or entrance window. For the helium detector and the LiF foils, this was determined by Eq. (6), which assumes an infinitely thick material. If penetration occurred, the probability of detection was ascertained from the neutron's velocity in that material, along with the absorption cross section and surface density of the absorber. For detection efficiency, a $1/v_{\text{relative}}$ dependence for the cross section was assumed. In the helium detector, this relative velocity was dominated by the velocity of the gas molecules, which, in effect, made the efficiency constant with respect to UCN velocity, whereas the net motion for the ⁶Li and ¹⁰B atoms was assumed to be zero for the converter foils.

The implantation profile of ¹⁰B into vanadium is quite different than the simple “infinite” step distribution of LiF; therefore detection was determined by calculating the reflection and transmission through a finite, complex square potential (a generalization of Eq. (6) for a finite width barrier). If the neutron was neither reflected nor transmitted, it was counted as absorbed. However, because of the high ¹⁰B absorption cross

section, the dominating factor in the ¹⁰B/V foil efficiency was the imaginary component of the cutoff velocity, v_i , not the shape of its implantation profile. Detailed Monte Carlo calculations showed negligible differences between the realistic implantation profile and a finite step, so we used the latter.

Then, for each type of detector, if the neutron was absorbed by its respective material, it was assumed that the efficiency for detecting the charged particles was 100%. In practice, this would simply change the overall normalization. The final detection rate was simply the number of counts relative to an initial number of 10^7 neutrons, with the overall normalization as a free parameter. In each case, the value of v_i calculated from the absorption cross section was assumed for each detection barrier. Also, if the neutrons were not absorbed in the foil, they were allowed to reflect off the nickel barrier using Eq. (6) and transported back through the LiF or ¹⁰B/V. During this second pass through the foil, the neutrons could also be absorbed.

5.1. Results

The helium detector data were used to determine the values of four simulation parameters: the initial angular distribution and the specularity of the shaper, the straight guides, and the curved guides. In addition to its high rate, this detector was chosen because it is often used to detect UCNs and is relatively well understood. In its “up” and “down” positions, the angular distribution was radically different, providing a robust check of the guide parameters. A four-dimensional parameter space was covered with 4000 simulations of the helium data to ascertain the best fit parameters, which were taken from the simulation yielding the lowest χ^2 . The initial angle was varied from 1° to 22° with intervals varying from 1° to 5°, and each of the three sets of specularity parameters (for the shaper, straight, and curved guides) was varied from ~75% to 100% in steps of 2.5%. The results of the simulation calibration studies on the helium data can be seen as curves in Fig. 10, which have a combined χ^2 of 4.0 for 11 degrees of freedom. The final values of the cutoff velocities for our foils are fairly insensitive to the exact parameter set chosen, with the stipulation that the set yields a reasonable χ^2 value for the helium data, which proves the robustness of our model.

Using the parameters fixed by the helium calibration and the average values of the surface densities measured by the elastic proton backscatter, the real part of the LiF and ¹⁰B/V foils' cutoff velocities was determined by simulating a wide range of cutoffs and extracting the pair that yielded the best fit to the data. The foils were analyzed together in order to maintain the relative yields dictated by the data shown in Fig. 11. For each LiF–¹⁰B/V cutoff velocity pair, the value of the normalization between data and simulation was determined by minimizing the χ^2 . Fig. 13 plots each minimum value of χ^2 as a function of both cutoff velocities with a grid spacing of 0.5–1.0 cm/s around the absolute minimum. Clearly, the cutoffs of the two foils are highly correlated. The final values for the true cutoffs were taken from the point with the absolute minimum value of $\chi^2 = 15.6$, for 11 degrees of freedom.

The statistical uncertainties seen in Fig. 13 as increasing values on each contour are small, leaving the overall uncertainties dominated by systematics associated with the simulation parameters. As mentioned above, contributions from specularity parameters and initial angle are negligible; contributions from uncertainties in neutron absorber density and from the value of the stainless steel cutoff are not. To estimate these uncertainties, a battery of simulations was performed in the following manner: for each simulation we changed one parameter, at a bracketing value, and minimized the χ^2 as described above to estimate the LiF and ¹⁰B/V cutoff velocities given the new parameter value.

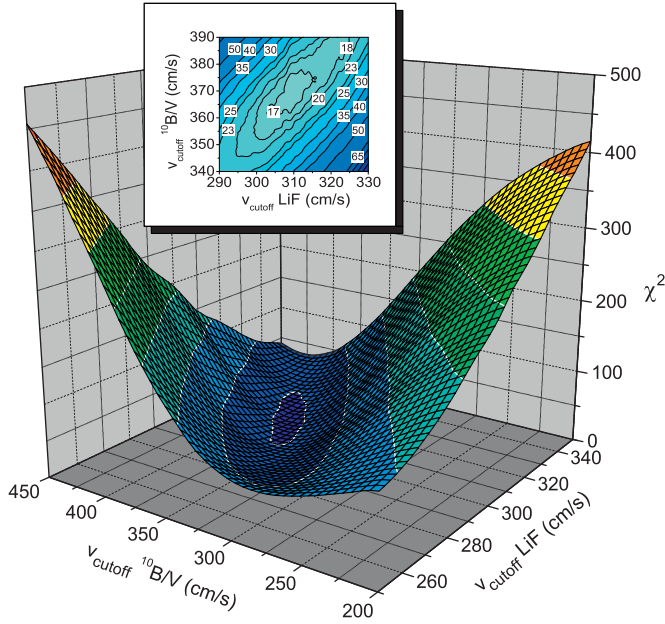


Fig. 13. χ^2 plot for LiF and $^{10}\text{B}/\text{V}$ cutoff velocities. The inset is an expanded view of this plot around the absolute minimum, with the values for the χ^2 printed along each contour line.

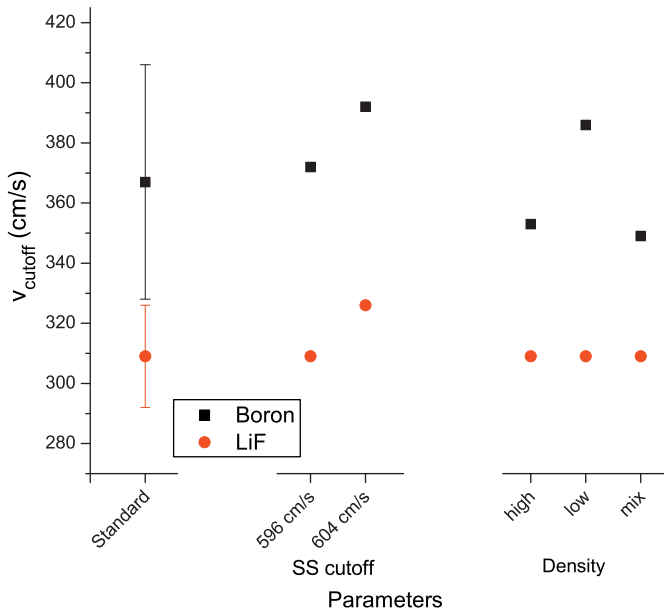


Fig. 14. Cutoff velocity as a function of simulation parameters, including the standard parameters and their systematic uncertainties. The mix density parameter combined the high neutron absorber density for LiF with the low neutron absorber density for $^{10}\text{B}/\text{V}$.

The bracketing values of the gravitational spectrometer parameters were chosen to increase the absolute minimum χ^2 of the helium calibration by ~ 4.0 , corresponding to a 95% confidence interval. The bracketing values of the area density of the neutron absorbers in the LiF and $^{10}\text{B}/\text{V}$ detectors were given by the uncertainty in the proton scattering measurements. A plot of the central values for the cutoffs determined from these minimizations is shown in Fig. 14, along with the final uncertainties determined from systematic errors. These uncertainties for the foils were obtained by adding in quadrature the difference between the standard value and each bracketing value. We find a cutoff velocity (effective potential) of

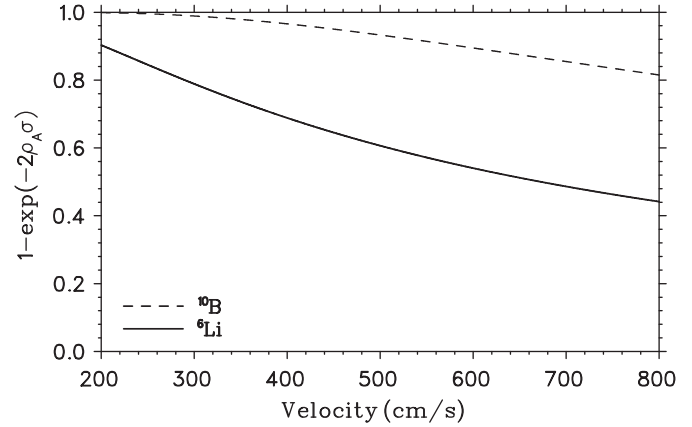


Fig. 15. Factor $1 - \exp(-2\rho_A\sigma)$ for the LiF and $^{10}\text{B}/\text{V}$ foils. The factor of 2 on the exponent is due to the fact that UCNs reflect on nickel.

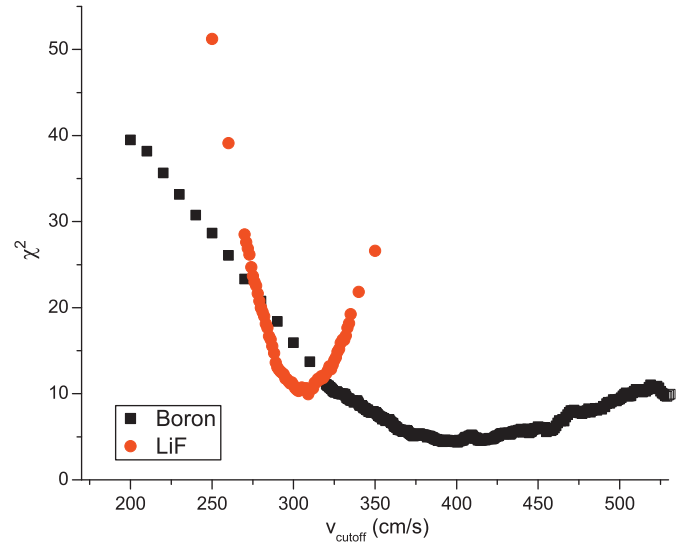


Fig. 16. χ^2 as a function of cutoff velocity for separate foil minimizations.

$309 \pm 17 \text{ cm/s}$ ($49.8 \pm 2.7 \text{ neV}$) for the LiF foils and $367 \pm 39 \text{ cm/s}$ ($70.3 \pm 7.5 \text{ neV}$) for the $^{10}\text{B}/\text{V}$ foils.

One can get some insight on the origin of the larger uncertainty for the $^{10}\text{B}/\text{V}$ foil by looking at its theoretical efficiency compared to LiF as shown in Fig. 15. Because the absorption probability scales as $1 - \exp(-2\rho_A\sigma_T v_T/v)$ (where $v_T = 2200 \text{ m/s}$ is the velocity for thermal neutrons, and σ_T is the corresponding absorption cross section) and because of the larger value of $\rho_A\sigma_T$ for the $^{10}\text{B}/\text{V}$ foils compared to the LiF foils ($\rho_A\sigma_{^{10}\text{B}/\text{V}} = 0.0061$, $\rho_A\sigma_{\text{LiF}} = 0.0021$), the efficiency of the LiF foils decreases with velocity faster than the efficiency of the $^{10}\text{B}/\text{V}$ foils. As a consequence, the gravitational spectrometer measurements are less sensitive to the cutoff velocity of the $^{10}\text{B}/\text{V}$ foils than the LiF foils. This is evident in Fig. 16, where the cutoff velocities of the two foils were considered separately. Therefore, although the $^{10}\text{B}/\text{V}$ foils were more efficient for UCN detection than the LiF foils, they were not ideal for determining of the cutoff velocity.

Although the determined cutoff for the LiF foils is consistent with the expected value within uncertainties, the determined cutoff for the $^{10}\text{B}/\text{V}$ foils is significantly greater than the value calculated from the scattering length, see Table 1. In the spectrum from elastic proton backscattering for $^{10}\text{B}/\text{V}$, carbon contamination is visible. Reasons for this contamination include cracking carbon onto the foils during implantation due to hydrocarbonates

present in the imperfect vacuum. This would be mostly on the surface and due to its high cutoff velocity ($v_{\text{graphite}} \sim 6 \text{ m/s}$, $V_F \sim 200 \text{ neV}$ through $v_{\text{diamond}} \sim 8 \text{ m/s}$, $V_F \sim 300 \text{ neV}$) is the likely explanation for the higher cutoff velocity. The other contaminants were already present in the nickel substrates before fabrication, which was determined by analyzing a blank foil and can be seen as shaded areas in Fig. 6.

6. Summary

We fabricated UCN detectors consisting of natural LiF and $^{10}\text{B}/\text{V}$ converter foils paired with silicon surface barrier detectors. The UCN detectors were taken to the ILL to determine the velocity below which the neutrons are undetectable due to surface reflection. Simulating the gravitational spectrometer used in the experiment, in addition to measuring the foils' area density via elastic proton backscattering, the cutoff velocities (effective potentials) were determined to be $309 \pm 17 \text{ cm/s}$ ($49.8 \pm 2.7 \text{ neV}$) for the natural LiF foils and $367 \pm 39 \text{ cm/s}$ ($70.3 \pm 7.5 \text{ neV}$) for the $^{10}\text{B}/\text{V}$ foils. Our measurements indicate that one can relatively easily produce smaller UCN detectors with cutoffs comparable to that of conventional ^3He detectors that have no danger of helium leaks.

References

- [1] R. Golub, D.J. Richardson, S.K. Lamoreaux, *Ultra-Cold Neutrons*, Adam Hilger, Bristol, UK, 1991.
- [2] C.A. Baker, et al., *Phys. Rev. Lett.* 97 (2006) 131801.
- [3] S. Arzumanov, et al., *Phys. Lett. B.* 483 (2000) 15.
- [4] A. Serebrov, et al., *Phys. Lett. B* 605 (2005) 72.
- [5] W. Mampe, et al., *JETP Lett.* 57 (1993) 82.
- [6] A. Saunders, et al., *Phys. Lett. B.* 593 (2004) 55.
- [7] T.M. Ito, Neutron beta decay: status and future of the asymmetry measurement, in: *Proceedings for CKM2006, the 4th International Workshop on the CKM Unitarity Triangle*, Nagoya, Japan, December 2006, arXiv:0704.2365 [nucl-ex].
- [8] B. Plaster, et al., *Nucl. Instr. and Meth. A* 595 (2008) 587.
- [9] R.W. Pattie Jr., et al., *Phys. Rev. Lett.* 102 (2009) 012301.
- [10] G.F. Knoll, *Radiation Detection and Measurement*, Wiley, New York, 1989.
- [11] C.A. Baker, et al., *Nucl. Instr. and Meth. A* 487 (2002) 511.
- [12] T. Kawai, et al., *Nucl. Instr. and Meth. A* 378 (1996) 561.
- [13] P. Maier-Komor, et al., *Nucl. Instr. and Meth. A* 480 (2002) 109.
- [14] V.K. Ignatovich, *The Physics of Ultracold Neutrons*, Oxford Clarendon Press, Oxford, UK, 1990.
- [15] V.F. Sears, *Neutron News* 3 (1992) 29.
- [16] (<http://www.canberra.com/products/497.asp>).
- [17] A.F. Gurbich, *Nucl. Instr. and Meth. B* 136–138 (1998) 60.
- [18] A. Cacioli, et al., *Nucl. Instr. and Meth. B* 249 (2006) 95.
- [19] M. Chiari, et al., *Nucl. Instr. and Meth. B* 184 (2001) 309.
- [20] A. Steyerl, et al., *Phys. Lett. A* 116 (1986) 347.
- [21] V.I. Morozov, et al., *JETP Lett.* 46 (1987) 377.
- [22] A. Steyerl, *Z. Phys.* 254 (1972) 169.